ACS OMEGA

http://pubs.acs.org/journal/acsodf

Article

Ferrate(VI) Oxidation Mechanism of Substituted Anilines: A Density Functional Theory Investigation

Hang Yu,* Yu Tian, Shuyue Wang, Xin Ke, Rundong Li, and Xiaohui Kang

Cite This: *ACS Omega* 2021, 6, 14317−14326

Read Online

ACCESS | Metrics & More | Article Recommendations | Supporting Information

ABSTRACT: Ferrate(VI) (Fe(VI)) is a promising oxidant coagulant and disinfectant for the degradation of organic micropollutants. However, it is hard to elucidate the detailed oxidation mechanism through the current experimental approaches. Substituted anilines (SANs) are important chemical compounds that are widely used in many industries. This paper presents the use of density functional theory (DFT) to understand the oxidation mechanism of SANs by Fe(VI) and the effect of substituents. The calculation results revealed that the primary oxidations of SANs follow the hydrogen atom transfer (HAT) mechanism. Interestingly, the hydroxyl oxygen of $HFeO_4^-$ is more reactive than the carbonyl oxygen when reacting with SANs. The formation of the SAN radical is crucial, and all of the products are formed from it. Azobenzene is more favorable to generate the above products. In addition, the obtained results indicate that this kind of substituent has a much greater influence on the reaction rather than the position. Thus, the present study provides a valuable insight into the transformation pathways of SANs in the Fe(VI) oxidation process and the effects of the substituent on oxidation. These results will advance the understanding of Fe(VI) involved in wastewater treatment.

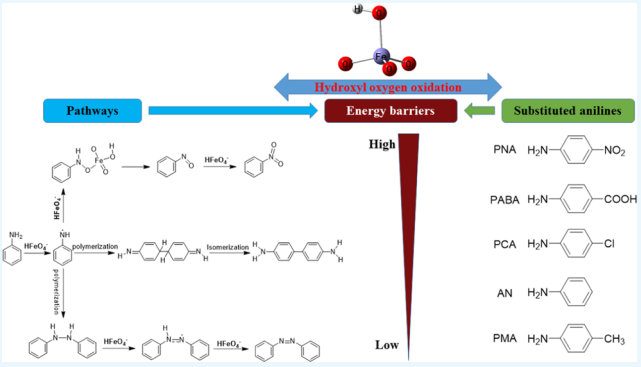

INTRODUCTION

Substituted anilines (SANs) are important chemical compounds, which are widely used in the production of dyes, rubber, medicine, pesticides, plastics, and paints. However, the wastewater discharged from these industries has become a serious environmental problem.[1] SANs can damage the central nervous system, cardiovascular system, liver, and kidneys of animals. Taking into account the hazards of SANs, SANs and their derivatives have received widespread attention as environmental pollutants in most countries.[2,3] In China, the allowable limits on SANs are very strict and they must not be detected.[3,4] Previous studies have shown that some oxidants, such as ozone and manganese dioxide, can effectively treat SANs.[2,5,6]

Recently, ferrate(VI) (Fe(VI)) has attracted increasing attention of researchers. Fe(VI) is a strong oxidant across the whole pH range with the reduction potentials varying from 2.20 to 0.7 V in acidic and alkaline conditions, respectively.[7] It has a good oxidation effect in a wide pH range during the process of wastewater treatment,[8,9] such as the removal rate of bisphenol A oxidized by Fe(VI) at pH 7 reached 97.5%.[7] Unlike ozone, Fe(VI) does not react with bromide ions and is not easy to form carcinogenic bromate ions.[10] In the oxidation process, Fe(VI) is reduced to nontoxic iron trioxide and iron hydroxide, and these two compounds are effective coagulants for removing toxic metals and organics.[11] Meanwhile, Fe(VI) has an efficient disinfection effect, which can quickly inactivate *Escherichia coli*.[12] Moreover, Fe(VI) can effectively destroy the sludge structure and improve the sludge dewatering performance.[13] Therefore, as an environmentally friendly chemical for oxidation, coagulation, and disinfection, Fe(VI) is suitable for multipurpose treatment of drinking water and wastewater.

The experiments of Huang et al. showed that the amino hydrogen atom of aniline (AN) first reacted with Fe(VI), and the product of azoaniline was detected.[14] Sun et al. found that SANs reacted with Fe(VI) quickly and detected the products such as azobenzene, nitrobenzene, and nitrosobenzene in their experiments.[15] They also proposed possible routes for the reaction as shown in Figure 1. But, so far, due to the rapid oxidation process and experimental difficulties in capturing unstable intermediates, it has not been clearly verified and structurally characterized, and the oxidation mechanisms of Fe(VI) and SANs have not yet been completely determined. A large number of experiments and calculations have been conducted on the reaction mechanism and products between Fe(VI) and a variety of environmental micropollutants (for

Received: March 2, 2021
Accepted: May 12, 2021
Published: May 25, 2021

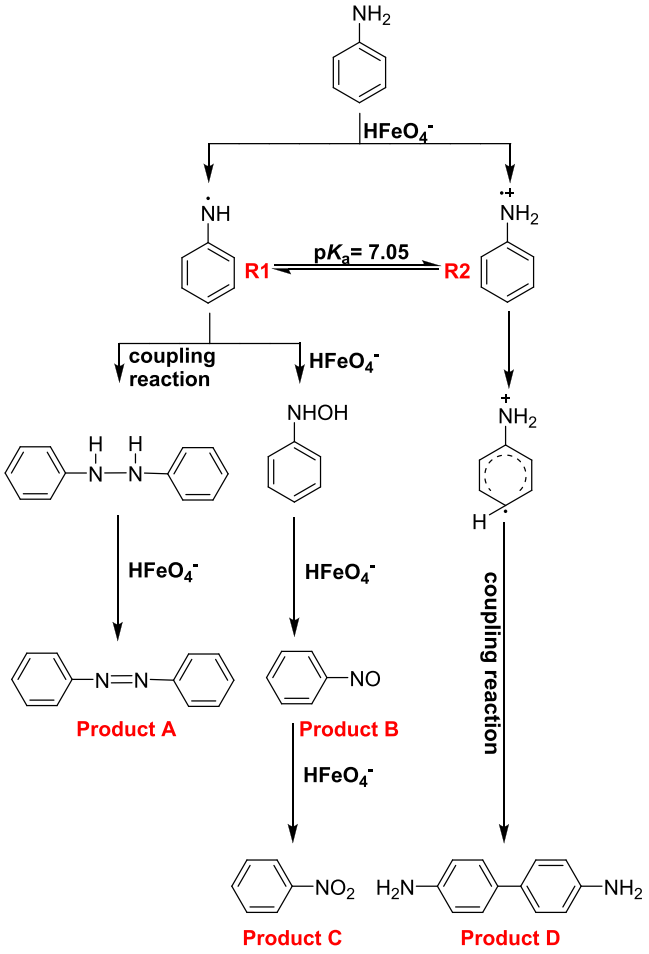

Figure 1. Possible pathways for Fe(VI) oxidation of aniline (AN).

example, drugs, nitrogen-containing compounds, and alcohols), showing that organic micropollutants contain electron-rich parts (for example, phenol, sulfonamide) and have high reactivity with Fe(VI).[16,17] Previous studies have shown that the oxidation of organic micropollutants by Fe(VI) has two possible reaction mechanisms, direct H atom abstraction and O atom transfer process, in which the iron substrate complex formed by the electrophilic attack of Fe(VI) is the key step of the reaction.[18] Johnson et al. experimentally speculated that Fe(VI) acts as a two-electron oxidant, and the oxidation of hydroxylamine occurs through organometallic intermediates with the Fe−N interaction.[19] Xie et al. speculated that the oxidation of methanol and ethanol by Fe(VI) follows the hydrogen atom transfer (HAT) mechanism.[17] Kamachi et al. showed that the oxygen oxidation of alcohol by Fe(VI) follows the HAT mechanism.[20] Yang et al. experimentally speculated that Fe(VI) is involved in both single-electron transfer (SET) and double electron transfer during the oxidation of ciprofloxacin and enrofloxacin.[21] At the same time, numerous studies have shown that the kind and position of the substituents affect the physicochemical properties of the compound and then affect the reaction mechanism.[22−25] At present, there have been no studies on the effect of the type and position of ring substituents on the reaction mechanism of SANs and Fe(VI).[23,24,26−28]

Density functional theory (DFT) calculations are widely adopted to interpret experimental findings and provide theoretical understanding.[29−31] The results obtained from quantum chemistry calculations can clearly describe the molecular structure and electronic properties for use in chemical transformation processes.[32] Therefore, all of the results in this paper are calculated by DFT. First, this paper revealed the degradation mechanism of aniline oxidized by Fe(VI). Then, the critical step of oxidation is proposed. In the following theoretical calculation, the effects of different substituents of methyl, chloride, carboxyl, and nitro on the reaction of substituted anilines with Fe(VI) were studied by the DFT, and the ortho, meta, and para positions of anilines were replaced with chlorine substituents to compare the effects of different positions of chlorine-substituted anilines on Fe(VI) oxidation of SANs. The effect of hydroxyl oxygen is higher than that of carbonyl oxygen. The intermediates are obtained in the reaction process, and the effect of the degradation intermediates is also evaluated. These results are of great significance for clarifying the oxidation mechanism of Fe(VI) oxidation of organic micropollutants and predicting degradation intermediates and products.

COMPUTATIONAL DETAILS

Model Species. The AN equilibrium is AN ⇌ AN^- + H^+ (pK_a = 4.63) and the pK_a values of other SANs are about 5; therefore, the SANs coexist with their anionic forms under neutral conditions.[2,33,34] Under neutral conditions, the main species of Fe(VI) include the monoprotonated species ($HFeO_4^-$) and the deprotonated species (FeO_4^{2-}) with respect to the equilibrium $HFeO_4^-$ ⇌ FeO_4^{2-} + H^+ (pK_a = 7.3 ± 0.1).[35] The experimental results of Norcross et al. showed that when the pH is lower than 9, the reaction rate increases with the increase of acidity and the protonation of Fe(VI) ions improves the oxidation ability of ethanol.[36] Sun et al. also showed that when the pH is lower than 10, the reaction rate increases with the increase of acidity, and the protonation of Fe(VI) ions improves the oxidation ability to SANs.[15] Previous experiments indicated that under neutral pH conditions, the reaction of $HFeO_4^-$ with SANs have higher rate constants in comparison with that of their other forms.[14,15] Due to the electrostatic repulsion between the two anions, it is expected that the complexation of $HFeO_4^-$ and substituted aniline anions ($SANs^-$) will be difficult. This paper did not study the mixture of anionic $SANs^-$ and $HFeO_4^-$. For these reasons, the research objects in the DFT calculations in this study are $HFeO_4^-$ and SANs.

DFT Calculations. All of the calculations presented in this work were performed using the Gaussian 16 program package.[37] The unrestricted formalism of B3LYP, which has shown good performance in the calculations of main group elements and metal oxides,[38] was used for open-shell calculations. In fact, the B3LYP functional has been proven to be reliable and effective for calculating the chemical reactions involved in various open-shell iron complexes, and it has been successfully applied to Fe(VI) oxidized organic substances.[20,38,39] The Wachters+f basis set was applied to optimize Fe atoms, and the 6-31+G(d,p) basis set was applied to optimize other atoms. This basis set combination is called BSI. To obtain more accurate energy, the single-point energy calculations were carried out based on the optimized geometry of the gas phase. The basis set of Fe atoms is the same as that in BSI, while for nonmetal atoms, the larger basis set 6-311++G (3df, 2pd) was used. Such a basis set combination is called BSII. The solvent effect was described by the SMD solvent model in the water environment.[30,40] To verify the accuracy of

https://doi.org/10.1021/acsomega.1c01134
ACS Omega 2021, 6, 14317−14326

the computational method, the author compared the lowest energy-optimized configurations of FeO_4^{2-} and $HFeO_4^-$ and AN in the gas phase (shown in Figure S1). The obtained structure is very consistent with the K_2FeO_4 and AN structures of the X-ray scan.[41,42] The related structure of the liquid-phase optimization (shown in Figure S2) is similar to the gas phase structure. Moreover, M06 and M06−2X functionals are selected to calculate the energy change, respectively (shown in Table S1). The most favorable pathway drawn by the M06 and M06−2X functionals are consistent with the conclusion in B3LYP. At the same time, it is found that the trends shown by the liquid phase and the gas phase are consistent (shown in Table S2). Therefore, all structures in this paper were optimized by the B3LYP method in the gas phase. The energy information was described at the B3LYP/BSII(SMD)//B3LYP/BSI level based on the geometry of gas-phase optimization.

The natural population analysis was performed by calculating the natural bond orbital (NBO) at the same level as the single-point energy calculation. Vibration frequency analysis was performed at the BSI level to obtain thermodynamic corrections and determine the nature of the stagnation point as a minimum value (zero imaginary frequency) or a transition state (only one imaginary frequency). The transition state (TS) was obtained through a two-step process: (1) the relax scan calculation, which was performed to show the TS region, and (2) the subsequent geometrical optimization toward the TS, which was carried out to obtain the TS structure. The structure of the product detected by the experiments was also very helpful for the preliminary estimation of the binding site in the initial TS geometry. Each transition state was verified to connect the designated reactant and product by performing an intrinsic reaction coordinate (IRC) calculation. The transition state activation free-energy barrier of electron transfer was calculated by Marcus theory.[43]

RESULTS AND DISCUSSION

Pathways for the Initial Oxidation of AN by $HFeO_4^-$. According to the products detected by Sun and Huang, it is assumed that $HFeO_4^-$ first reacts with the amino hydrogen on AN.[14,15] Feng et al. also found that the amino part of aniline was more reactive.[44] This is due to the unshared electron pair on the nitrogen atom of the amino group, which can interact with the π electron on the benzene ring. A conjugated system is formed and electron delocalization occurs. As a result, the electron cloud density of nitrogen atoms is reduced, which weakens the bond energy of amino N−H. The energy gap between the lowest unoccupied molecular orbital (LUMO) of $HFeO_4^-$ and the highest occupied molecular orbital (HOMO) of AN is 2.35 eV, which is smaller than the energy gap of 6.85 eV between LUMO of AN and the HOMO of $HFeO_4^-$ (shown in Figure S3). Therefore, electrons should be transferred from AN to $HFeO_4^-$. The four pathways of the initial reaction of $HFeO_4^-$ with the amino group of AN were studied (shown in Figure 2). Both Path 1 and Path 2 generate AN radicals through the H atom (HAT) mechanism. Path 1 is the carbonyl oxygen (shown in Figure S1, labeled 2, 3, 4) attacking $HFeO_4^-$ and generating $H_2FeO_4^{\bullet-}$. Path 2 is the hydroxy oxygen (shown in Figure S1 labeled 1) attacking $HFeO_4^-$ and generating $H_2O{\cdot}FeO_3^{\bullet-}$. In contrast, the activation free-energy barrier for Path 2 is 3.5 kcal/mol lower than Path 1. Path 3 is a single-electron transfer (SET)

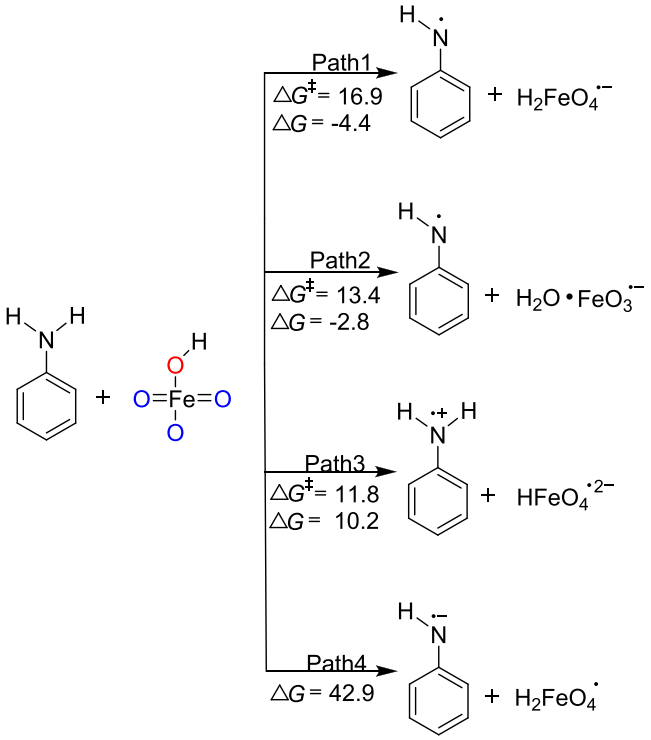

Figure 2. Free-energy profiles (ΔG, kcal/mol) and activation free-energy barriers ($\Delta G^{\ddagger}$, kcal/mol) for four possible pathways (red: hydroxyl oxygen; blue: carbonyl oxygen).

path. According to the theory of Marcus,[43,45,46] the reaction activation free-energy barrier is 11.8 kcal/mol and the reaction energy absorption is 10.2 kcal/mol. Path 4 is the path of proton transfer. Since the transition state of proton transfer is the same as in the transition state of atom transfer, it is speculated that the transition state is not a proton transfer transition state by observing the charge transfer during the transition state. The absorption energy of the reaction in path 4 was calculated to be 42.9 kcal/mol, which is thermodynamically unfavorable and, therefore, no further consideration is needed. In summary, from the perspective of kinetics and thermodynamics, H atom extraction (HAT) is easy to occur, and hydroxyl oxygen extraction is more advantageous for H atoms. It is consistent with previous results that protonated Fe(VI) is more likely to react.[36] The oxidizing ability of Fe(VI) species became stronger upon protonation because of the increased electron-accepting ability of $HFeO_4^-$.[47] According to the properties of AN and $HFeO_4^-$ and previous studies on the reaction, the possible path of the reaction between AN and $HFeO_4^-$ is shown in Figure 1.[15,48−50] First, AN forms AN radical R1 through the HAT mechanism or AN radical cation R2 by the SET mechanism. Then, two radicals R1 dimerize to azobenzene (Product A). In addition, the radical cation R2 can also be converted by resonance and then coupled to produce biphenyl (Product D). When $HFeO_4^-$ is in excess, the N of R1 may undergo hydroxylation to form phenylhydroxylamine, and its further oxygenation can lead to the generation of nitrosobenzene (Product B) and nitrobenzene (Product C).

Comparison of Two Pathways of the HAT Mechanism. The previous analysis shows that the HAT mechanism of AN to form an AN radical (R1 in Figure 1) is more suitable for the reaction of AN and $HFeO_4^-$. Since most of the previous studies on Fe(VI) used FeO_4^{2-} as the research object and

https://doi.org/10.1021/acsomega.1c01134
ACS Omega 2021, 6, 14317−14326

mainly analyzes the oxidation mechanism of the carbonyl oxygen of Fe(VI) on organic matter.[17,51,52] We first tested the attack pathway of Fe(VI) carbonyl oxygen (Path 1 in Figure S4). As shown in Figure S4, $HFeO_4^-$ has a tetrahedral geometry and interacts with AN to form the complex ^{3}**1A1**. Moreover, ^{3}**1A1** undergoes an electrophilic attack by $HFeO_4^-$ on the H atom of AN via a transition state ^{3}**TSA$_{1-2}$**, leading to ^{5}**2A1**, and then it yields R1. The experimental result of Sun et al. also shows that when the pH is lower than 10, the reaction rate increases with the increase of acidity.[53] The protonation of Fe(VI) increases the oxidation ability of AN.[8,53,54] We tested the attack pathway of the Fe(VI) hydroxyl oxygen (Path 2 in Figure S4). It is very clear that Path 2 has a lower activation free-energy barrier, and the Path 2 product $H_2O{\cdot}FeO_3^{\bullet-}$ can be converted to $H_2FeO_4^-$ (shown in Figure S5). Similar structures of H_2O complexes have been proposed in the previous study.[55,56] To illustrate the inner reason for this priority, the transition state energy decompositions[57,58] were carried out for the two paths. The transition states were divided into two fragments of unoxidized AN and $HFeO_4^-$, and the interaction energy (ΔE_{int}) and deformation energy (ΔE_{def}) between the two fragments were calculated. The interaction energy (ΔE_{int}) was estimated through the single-point energy of the transition state and the two fragments. These energies, together with the energy of the respective fragments in their optimal geometry, allow for the estimation of the deformation energies of the two fragments, AN fragment deformation energy ($\Delta E_{def\text{-}A}$) and $HFeO_4^-$ fragment deformation energy ($\Delta E_{def\text{-}Fe}$). The deformation energy (ΔE_{def}) of the transition state is the sum of the deformation energy of the two fragments. Bond dissociation energy (BDE) is the difference between the single-point energy of AN and the energy of hydrogen (0.5 au) and the single-point energy of AN without geometric optimization after dehydrogenation. The transition state activation free-energy barrier ($\Delta G^{\ddagger}$), AN fragment deformation energy ($\Delta E_{def\text{-}A}$), $HFeO_4^-$ fragment deformation energy ($\Delta E_{def\text{-}Fe}$), transition state deformation energy (ΔE_{def-TS}), interaction energy (ΔE_{int}), and bond dissociation energy (ΔE_{bond}) statistics are as shown in Table 1. The bond length information of the two transition state structures is shown in Figure S6. Previous studies have found that the reaction deformation energy (ΔE_{def}) caused by steric hindrance has an inhibitory effect on the reaction.[57,59] The greater the deformation energy (ΔE_{def}), the stronger the inhibition. However, the greater the interaction energy (ΔE_{int}) caused by internal electronic factors, the easier the reaction. Through calculations (shown in Table 1), Path 2 is more advantageous, which is mainly attributed to the stronger interaction (−30.5 kcal/mol for Path 1, −48.2 kcal/mol for Path 2). The intrinsic electronic factors have a greater impact on the transition states. It is found that the spin density of the two transition states varies greatly (shown in Table S3). Path 2 has a larger spin density than Path 1. The result of larger spin density increased the oxidation ability.[44] Furthermore, the transition state of Path 2 probably formed the antiferromagnetic coupling.[60] Previous studies have shown that antiferromagnetic coupling makes the electron delocalization more obvious, and then forms a more stable transition state.[60,61] Therefore, the hydroxyl oxygen attack of $HFeO_4^-$ is easier than the attack of carbonyl oxygen. In this study, each step of the reaction involving the competition between the carbonyl oxygen and hydroxyl oxygen was calculated and the more competitive path was selected.

Table 1. Energy Decomposition Analyses (kcal/(mol mol)) for the Transient States in Two Pathways to Abstract the H Atom

	$\Delta G^{\ddagger}$	ΔE_{bond}	$\Delta E_{def\text{-}A}$	$\Delta E_{def\text{-}Fe}$	$\Delta E_{def\text{-}TS}$	ΔE_{int}
path 1	16.9	101.5	36.9	3.1	40.0	−30.5
path 2	13.4	97.0	46.7	7.3	54.0	−48.2

Formation Pathway for Product A. The formation pathway for Product A is shown in Figure 3. Taking the AN radical as the initial reactant, first, the two AN radicals generate an NH−NH bond through the polymerization reaction. This is a process of incompetence that can easily occur. Then, the hydroxyl group in $HFeO_4^-$ abstracts the H in NH−NH. This is a process without the activation free-energy barrier through ^{3}**TS$_{1-2}$**. The presence of the prereaction complex[62] before the hydrogen pumping transition state reduces the reaction activation free-energy barrier. It can be seen from Figure 3 that the first H abstracting reaction releases 36.4 kcal/mol, and the reaction is easy to occur. Then, the newly added $HFeO_4^-$ continues to react with **M$_2$**, which is the same as the transition state of abstracting H in the last step. The transition state is also a process without an activation free-energy barrier. Overall, the reaction releases 87.1 kcal/mol and consumes two $HFeO_4^-$. The products are Product A and $H_2O{\cdot}FeO_3^{\bullet-}$.

Formation Pathways for Product B and Product C. First, $HFeO_4^-$ interacts with the AN radical to form a complex reactant ^{4}**3B**. Through the transition state ^{4}**TS$_{3-4}$**, the carbonyl oxygen in $HFeO_4^-$ is bonded with the N in the AN radical to form an N−O bond, and then forms the ^{4}**4B** complex product. By observing the activation free-energy barrier of ^{4}**TSB$_{3-4}$**, it is found that this is a process of intermediate activation free-energy barrier. After undergoing transition state ^{4}**TSD$_{4-5}$**, H is abstracted from the amino group and the Fe−O bond cleaves to form Product B. The reaction releases 55.9 kcal/mol and consumes one $HFeO_4^-$. The generation path of the hydroxyl product is shown in Figure S7. This path has a higher transition state energy barrier. The generation paths of Product B and Product C are complex. The formation pathway for Product B and Product C shown in Figure 4 is more suitable. In addition, Product B reacts with the carbonyl oxygen in $HFeO_4^-$ to generate Product C. ^{3}**6C** is formed by the H-bond and the H-bond gradually activates the Fe−O bond, as indicated by the gradually elongated Fe−O bond length. The cleavage of the activated Fe−O bond takes place through a transition state ^{3}**TSC$_{6-7}$**, yielding Product C. The activation free-energy barrier of the transition state of the reaction is 24.5 kcal/mol, which is 3.2 kcal/mol higher than that of Product B. Product C is also likely to be formed because of the heat released from the previous reaction. However, the difficulty of crossing the activation free-energy barrier between Product B and Product C is much higher than that of the previous production of Product A. The reaction path to produce azobenzene is more favorable.

Formation Pathways for Product D. The pathway proposed by Sun[15] to generate Product D is shown in Figure 5I. First, two AN molecules undergo SET to absorb 20.4 kcal/mol and generate AN cation radicals. Moreover, the two AN cation radicals undergo an addition reaction, and Product D is formed by H^+ ionization. Our proposed Product D path is shown in Figure 5II. Two AN molecules undergo HAT to release 22.4 kcal/mol and generate AN radicals. Then, the two

https://doi.org/10.1021/acsomega.1c01134
ACS Omega 2021, 6, 14317−14326

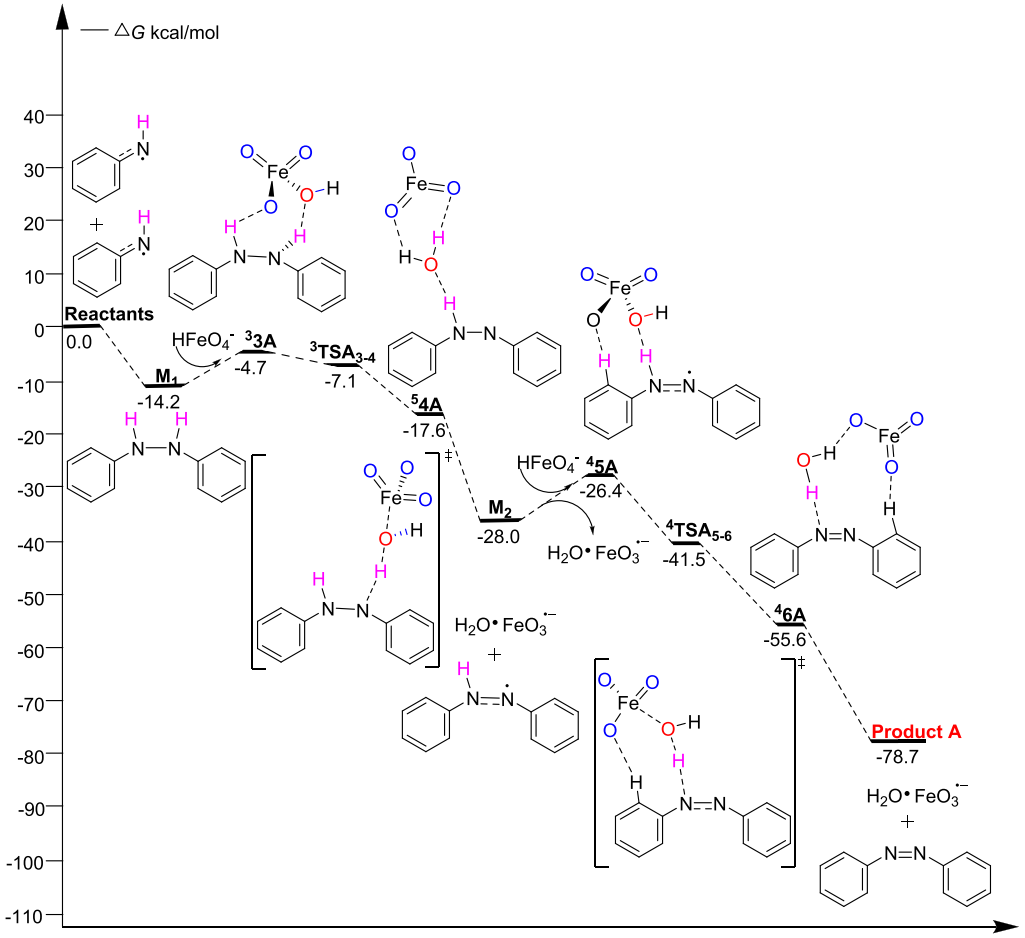

Figure 3. Computed free-energy profiles (kcal/mol) for the $HFeO_4^-$ oxidation of the AN radical to yield Product A. (The left superscript in the labeling of the stationary points denotes the corresponding spin multiplicity. The sign of the negative charge is not shown, and the same is true for the following figures).

AN radicals further undergo an addition reaction and absorb 7.7 kcal/mol. Finally, Product D is afforded through isomerization. Ultimately, it is found that the pathway shown in Figure 5II is more favorable through comprehensive comparison.

By comparing the activation free-energy barriers of each step of the reaction between AN and $HFeO_4^-$, it is found that the rate-determining step of the process is the first step of induced dehydrogenation reaction; therefore, the following studies been considered the first step of the dehydrogenation reaction of each SANs.

Substituent Effect. The structures of aniline (AN), *p*-methyl-substituted aniline (PMA), *p*-carboxyl-substituted aniline (PABA), *p*-nitro-substituted aniline (PNA), *p*-chloro-substituted aniline (PCA), *o*-chloro-substituted aniline (OCA), *m*-chloro-substituted aniline (MCA), and *o*-*p*-chloro-substituted aniline (OPDCA) are as shown in Figure S8. The AN, PMA, PABA, PNA, and PCA are selected to compare the effect of different substituents on the reaction of SANs with $HFeO_4^-$. The AN, PCA, OCA, and OPDCA are selected to compare the effect of the substituent position on the reaction of SANs with $HFeO_4^-$.

Effects of Different Substituents on the Initial Reaction of SANs with $HFeO_4^-$. Complete optimization of the possible structures of AN, PCA, PMA, PABA, and PNA finally results in the most stable structure. The obtained structure and electronic information are shown in Table S4. The related atomic number and position in Table S4 are shown in Figure 6. In terms of bond length, it can be seen that the substituent at the para position has no effect on the N−H bond length on the amino group, and the impact on the C−N bond length is also relatively small. In terms of bond angles, it is found that $A_{6-12-13}$ and $A_{6-12-14}$ change at the same time; therefore, the substituent of the para position has the same effect on the structure of the two H on the amino group. Furthermore, the methyl substituent reduces the bond angles of both $A_{6-12-13}$ and $A_{6-12-14}$ of SANs, while the other substituents increase, and the nitro group has the greatest change on them. The steric effect and electronic effect of the substituents will affect the structures of the substituted products.[63] When the substituent is the electron-donating nitro group, the positive charge of C_6 decreases and the negative charge of $N_{12}H_{13}H_{14}$ groups increases. When the substituent is the strong electron-withdrawing group, such as the nitro group and the carboxyl group, the charge of C_6 increases and the electronegativity of $N_{12}H_{13}H_{14}$ groups decreases. It is possible that the carboxyl group and the nitro group and the benzene ring form a $\pi-\pi$ conjugation effect, which shortens the R_{6-12} bond and increases the bond angles of both $A_{6-12-13}$ and $A_{6-12-14}$. In summary, it can be concluded that the para-substituent has the same effect on the two H of the amino group, and the charge of the C_6 and $N_{12}H_{13}H_{14}$

https://doi.org/10.1021/acsomega.1c01134
ACS Omega 2021, 6, 14317−14326

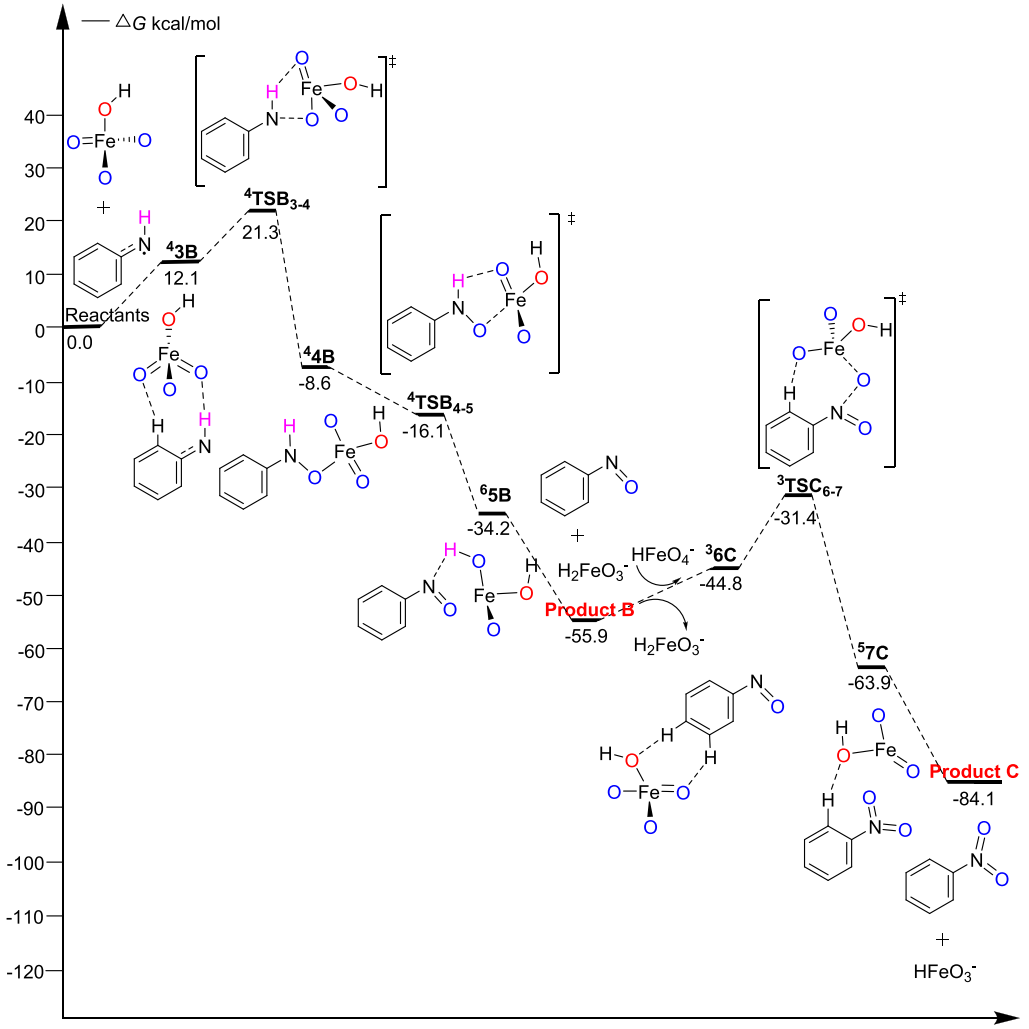

Figure 4. Computed free-energy profiles (kcal/mol) for $HFeO_4^-$ oxidation of the AN radical to yield Product B and Product C.

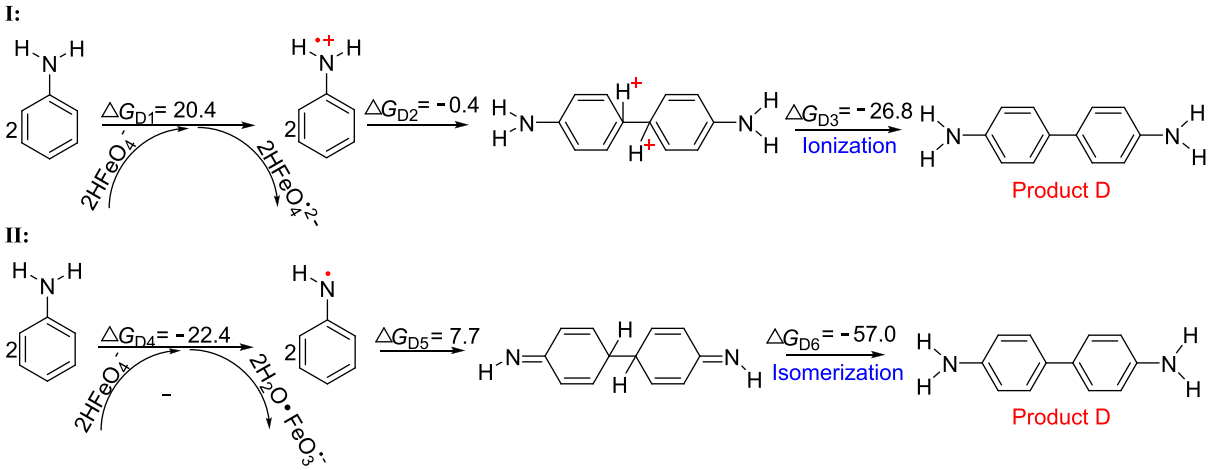

Figure 5. Computed possible pathway I and pathway II for Product D (kcal/mol).

groups is related to the electron-withdrawing and electron-donating abilities of the substituent.

Based on the reaction mechanism of $HFeO_4^-$ with AN and the products detected by Huang and Sun, it is assumed that $HFeO_4^-$ still reacts with amino hydrogen of SANs first.[14,15] The concentration position of the HOMO orbitals of the SANs remains unchanged. Furthermore, the HOMO orbitals are mainly concentrated on the benzene ring part on the amino side and the C at the para position of the amino group. The energy gaps between the LUMO of $HFeO_4^-$ and HOMO of SANs are smaller than the energy gaps between the LUMO of SANs and the HOMO of $HFeO_4^-$ (shown in Table S5). Hence, when the two undergo redox reactions, electrons should be transferred from SANs to $HFeO_4^-$. In addition, the

https://doi.org/10.1021/acsomega.1c01134
ACS Omega 2021, 6, 14317−14326

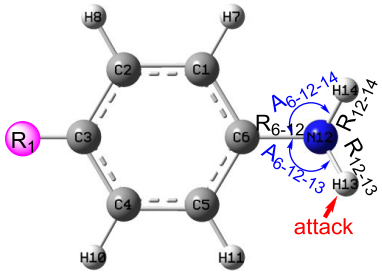

Figure 6. Structure and labels of SANs (R_1 is the substituent).

order of SANs E_{HOMO} is PMA > AN > PCA > PABA > PNA (shown in Table S5); therefore, the order of SAN electron-withdrawing ability is PNA > PABA > PCA > AN > PMA. The thermodynamic and kinetic data of the four initial mechanisms inferred from the reaction of $HFeO_4^-$ with amino H are shown in Table S6. It is found that hydroxyl oxygen abstracts H atoms from the amino of each SAN, which is the most dominant route. It shows that the SANs retain the initial reaction mechanism of AN with $HFeO_4^-$.

The activation free-energy barriers and experimental values of AN, PMA, PCA, PABA, and PNA are shown in Table S7. The calculated order of activation free-energy barriers is PMA < AN < PCA < PABA < PNA and the calculated result is the same as the experimental results of Sun.[15] The substitution of electron-withdrawing substituents, nitro, carboxyl, and chlorine, reduces the chemical reaction rates of SANs, while the reaction rate increases after the electron-donating substituent methyl is substituted. The order of SAN chemical reaction rates is the same as the order of E_{HOMO} (shown in Table S5). The activation free-energy barriers and bond dissociation energy statistics of each reaction are shown in Table S8. It can be seen that the bond dissociation energy has the same law as the activation free-energy barriers. To further explore the influencing factors of the transition state energy barrier, the decomposition statistics of the transition state energy of each initial reaction are shown in Table 2. For PMA and AN, the

Table 2. Energy Decomposition Analyses for the Transition State in the Initial Reaction Pathways between Para-Substituent Anilines and $HFeO_4^-$ (kcal/mol)

	PMA	AN	PCA	PABA	PNA
$\Delta E_{def\text{-}A}$	44.4	46.7	49.2	48.7	48.6
$\Delta E_{def\text{-}Fe}$	7.1	7.3	7.3	8.0	8.6
$\Delta E_{def\text{-}TS}$	51.6	54.0	56.5	56.7	57.2
ΔE_{int}	−47.9	−48.2	−50.4	−46.2	−31.7

interaction energies of TS_{PMA} (transition state of PMA reacts with $HFeO_4^-$) and TS_{AN} are similar; therefore, the transition state deformation energy plays an important role in TS_{PMA}, and it is mainly attributed to stronger deformation. The reason for the low activation free-energy barrier of PMA compared to AN is mainly due to the smaller deformation during the transition state, especially the smaller deformation of PMA fragments in the transition state. The transition state interaction energy difference between TS_{PMA} and TS_{AN} is −2.2 kcal/mol, the transition state deformation energies differ by 2.5 kcal/mol, which is mainly derived from PCA fragments. Consequently, the activation free-energy barrier of PCA is affected by the deformation and interaction, and the effect of deformation is greater than the interaction. Moreover, the deformation energies of TS_{PABA} and TS_{PCA} are relatively close, but the interaction energies are quite different. Therefore, the high activation free-energy barrier of PABA is mainly attributed to the effect of the interaction. It is obvious that the high energy barrier of PNA is also mainly due to the weak interaction. In summary, the deformation in PMA plays a greater role, the interaction in both PNA and PABA can play a greater role, and the interaction energy in PCA is similar to the deformation energy. In other words, the methyl substituent mainly affects the steric hindrance, the chlorine substituent is affected by steric hindrance and electronic factors, and the carboxyl substituent and nitro substituent are affected by electronic factors. The stronger the electron-withdrawing ability of the substituent, the slower the reaction rate.

The bond length of the key part of the transition state and charge difference between the transition state and the reactant are shown in Table S9. The related atomic number and position are shown in Figure 7. The deformation energy of different positions of each SAN is mainly concentrated in the amino part H_{13} and the O_{18} part of $HFeO_4^-$ fragments. The difference in interaction energy is mainly concentrated in the $N_{12}H_{13}H_{14}$ group of each SAN. In addition, the interaction of the transition state of PNA is also greatly affected by $HFeO_4^-$ fragments. In summary, the methyl substituent mainly reduces the steric hindrance of the amino part of the transition state when the PMA reacts with $HFeO_4^-$ and accelerates the initial reaction rate. However, PCA, PABA, and PNA are due to the increased steric hindrance of the amino part in the transition state and the change of the charge of the $N_{12}H_{13}H_{14}$ group, which results in the decrease of the initial reaction rate. Moreover, due to the large change in the charge on N_{12}, the initial chemical reaction rate of PNA changes significantly.

Effect of Substituent Positions on the Reaction of SANs with $HFeO_4^-$. Complete optimization of the possible structures of AN, PCA, OCA, MCA, OPDCA finally results in the most stable structures. The obtained structure and the electronic information are shown in Table S10. In terms of the bond length, it can be seen that the chlorine substituent at different positions has no effect on the N−H bond length on the amino group, and the effect on the C−N bond length is only 0.01 Å (shown in the structure of Table S10). In terms of bond angles, it is found that both the bond angles $A_{6-12-13}$ and $A_{6-12-14}$ of chlorine-substituted anilines increase slightly (shown in the structure of Table S10). Moreover, the farther the substitution position of the amino group, the smaller the effect on the amino bond angle; and two chlorine substituents can enhance the effect on the bond angle. The different positions of the substituents mainly caused the charge of the $N_{12}H_{13}H_{14}$ group to change, and the effect on the charge of the $N_{12}H_{13}H_{14}$ group gradually increased from the para position to the ortho position. In summary, the chlorine substituent at different positions has weak effects on the structure and charge of SANs, mainly affecting the bond angles $A_{6-12-13}$ and $A_{6-12-14}$ of SANs, as well as the charge of the $N_{12}H_{13}H_{14}$ group. The closer the substitution position to the amino group, the greater the effect on the amino bond angle and the charge of the $N_{12}H_{13}H_{14}$ group.

The concentration of the HOMO orbitals of chlorine-substituted anilines remains unchanged (shown in Table S11). The HOMO orbitals are mainly concentrated on the benzene ring part on the amino side and the C at the para position of the amino group. But for PCA and OPDCA, the HOMO distribution has been transferred to the Cl atom. The

https://doi.org/10.1021/acsomega.1c01134
ACS Omega 2021, 6, 14317−14326

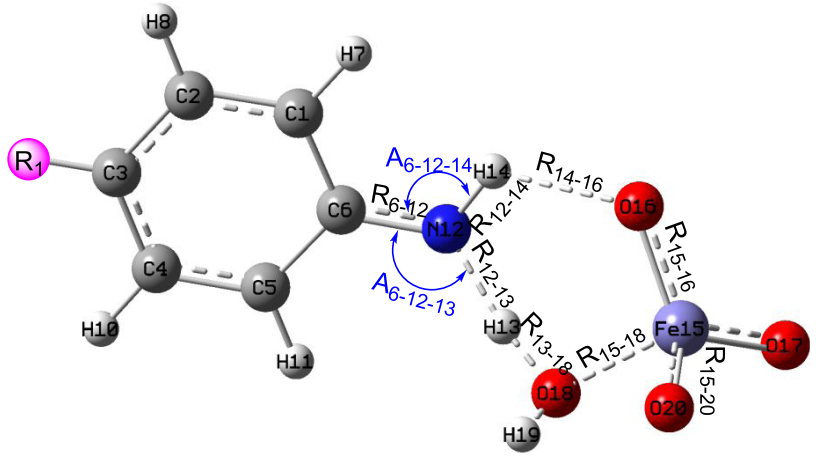

Figure 7. Structure and label of the transition state.

activation free-energy barriers and experimental values of AN, PCA, MCA, OCA, and OPDCA are shown in Table S12. The order of activation free-energy barriers is AN > PCA > MCA ≥ OCA > OPDA, and the calculated result is the same as the experimental results of Sun.[15] It can be seen that no matter where the chlorine substituent is, all reaction rates of SANs are reduced, and the different positions of the chlorine substituent had little effect on the activation energy of the initial reaction. The results indicate that this kind of substituent has a much greater effect on the reaction rather than the position.

CONCLUSIONS

In this work, we have reported on the DFT calculations of various important reactions involved in the oxidative degradation of AN. Computational results showed that HAT was the dominant mechanism for $HFeO_4^-$ to degrade AN. Moreover, the hydroxyl oxygen of $HFeO_4^-$ is more reactive than the carbonyl oxygen when reacting with AN. The potential mechanistic pathways to the formation of major degradation products of AN have been established. The formation of the AN radical was the rate-determining step of the reaction. In addition, the other SANs retained the initial reaction mechanism of AN with $HFeO_4^-$, still following the HAT mechanism. The electron-donating ability of the substituent had a great influence on the reaction, and the stronger the substituent of electronic donation, the more reactive are the SANs reacting with $HFeO_4^-$. The chlorine substituents at different positions had little effect on the activation energy of the reaction. As Fe(VI) represents a sustainable green oxidant and has been successfully applied in the degradation of trace organic pollutants, further studies are necessary to understand the mechanism of the reaction of Fe(VI) with other pollutants. The data presented here would shed new light on the understanding of the interaction mechanism of Fe(VI) with organic compounds and providing theoretical support for the better application of Fe(VI) in the degradation of organic matter.

ASSOCIATED CONTENT

Supporting Information

The Supporting Information is available free of charge at https://pubs.acs.org/doi/10.1021/acsomega.1c01134.

Supporting information contains additional tables and figures accompanying the manuscript. It includes the calculated structures, energies, charges, and spin densities (PDF)

AUTHOR INFORMATION

Corresponding Author

Hang Yu − *Liaoning Key Laboratory of Clean Energy and College of Energy and Environment, Shenyang Aerospace University, Shenyang, Liao Ning 110136, China;* orcid.org/0000-0002-5611-5849; Phone: (+86)024-89723947; Email: hangyu@sau.edu.cn

Authors

Yu Tian − *Liaoning Key Laboratory of Clean Energy and College of Energy and Environment, Shenyang Aerospace University, Shenyang, Liao Ning 110136, China*

Shuyue Wang − *Liaoning Key Laboratory of Clean Energy and College of Energy and Environment, Shenyang Aerospace University, Shenyang, Liao Ning 110136, China*

Xin Ke − *Liaoning Key Laboratory of Clean Energy and College of Energy and Environment, Shenyang Aerospace University, Shenyang, Liao Ning 110136, China*

Rundong Li − *Liaoning Key Laboratory of Clean Energy and College of Energy and Environment, Shenyang Aerospace University, Shenyang, Liao Ning 110136, China;* orcid.org/0000-0002-8669-5397

Xiaohui Kang − *College of Pharmacy, Dalian Medical University, Dalian 116044, China;* orcid.org/0000-0003-2793-7111

Complete contact information is available at: https://pubs.acs.org/10.1021/acsomega.1c01134

Notes

The authors declare no competing financial interest.

ACKNOWLEDGMENTS

This work was supported by a grant-in-aid from the National Key Research and Development Program of China (No. 2019YFC1903901) and the Scientific Research Foundation of the Educational Department of Liaoning Province (No. JYT2020043).

NOMENCLATURE

Fe(VI)	ferrate (VI)
SAN_S	substituted anilines

https://doi.org/10.1021/acsomega.1c01134
ACS Omega 2021, 6, 14317−14326

HAT	hydrogen atom transfer
DFT	density functional theory
NBO	natural bond orbital
TS	transition state
HOMO	the highest occupied molecular orbital
LUMO	the lowest unoccupied molecular orbital
SET	single-electron transfer
Product A	azobenzene
Product B	nitrosobenzene
Product C	nitrobenzene
Product D	biphenyl
$\Delta G^{\ddagger}$	transition state activation free-energy barrier
ΔE_{int}	interaction energy
ΔE_{def}	deformation energy
$\Delta E_{def\text{-}Fe}$	deformation energy of the $HFeO_4$ fragment
$\Delta E_{def\text{-}A}$	deformation energy of the aniline fragment
ΔE_{def-TS}	deformation energy of transition state
E_{bond}	bond dissociation energy
PMA	*p*-methyl-substituted aniline
PABA	*p*-carboxyl-substituted aniline
PNA	*p*-nitro-substituted aniline
PCA	*p*-chloro-substituted aniline
OCA	*o*-chloro-substituted aniline
MCA	*m*-chloro-substituted aniline
OPDCA	*o*-*p*-chloro-substituted aniline
TS_{PMA}	transition state of PMA reacts with $HFeO_4^-$

REFERENCES

(1) Lin, X.; Zhang, J.; Luo, X.; Zhang, C.; Zhou, Y. Removal of aniline using lignin grafted acrylic acid from aqueous solution. *Chem. Eng. J.* **2011**, *172*, 856−863.

(2) Tekle-Röttering, A.; von Sonntag, C.; Reisz, E.; Eyser, C. v.; Lutze, H. V.; Türk, J.; Schmidt, W.; Schmidt, T. C.; et al. Ozonation of anilines: Kinetics, stoichiometry, product identification and elucidation of pathways. *Water Res.* **2016**, *98*, 147−159.

(3) Liu, Y.; Zhang, H.; Sun, J.; Liu, J.; Shen, X.; Zhan, J.; Zhang, A.; Ognier, S.; Cavadias, S.; Li, P. Degradation of aniline in aqueous solution using non-thermal plasma generated in microbubbles. *Chem. Eng. J.* **2018**, *345*, 679−687.

(4) Wu, G.-Q.; Zhang, X.; Hui, H.; Yan, J.; Zhang, Q.-S.; Wan, J.-L.; Dai, Y. Adsorptive removal of aniline from aqueous solution by oxygen plasma irradiated bamboo based activated carbon. *Chem. Eng. J.* **2012**, *185*−*186*, 201−210.

(5) Salter-Blanc, A. J.; Bylaska, E. J.; Lyon, M. A.; Ness, S. C.; Tratnyek, P. G. Structure−Activity Relationships for Rates of Aromatic Amine Oxidation by Manganese Dioxide. *Environ. Sci. Technol.* **2016**, *50*, 5094−5102.

(6) Casero, I.; Sicilia, D.; Rubio, S.; Pérez-Bendito, D. Chemical degradation of aromatic amines by Fenton's reagent. *Water Res.* **1997**, *31*, 1985−1995.

(7) Han, Q.; Wang, H.; Dong, W.; Liu, T.; Yin, Y.; Fan, H. Degradation of bisphenol A by ferrate(VI) oxidation: Kinetics, products and toxicity assessment. *Chem. Eng. J.* **2015**, *262*, 34−40.

(8) Sharma, V. K.; Mishra, S. K.; Nesnas, N. Oxidation of Sulfonamide Antimicrobials by Ferrate(VI) [FeVIO42-]. *Environ. Sci. Technol.* **2006**, *40*, 7222−7227.

(9) Chen, J.; Qi, Y.; Pan, X.; Wu, N.; Zuo, J.; Li, C.; Qu, R.; Wang, Z.; Chen, Z. Mechanistic insights into the reactivity of Ferrate(VI) with phenolic compounds and the formation of coupling products. *Water Res.* **2019**, *158*, 338−349.

(10) Zhang, T. Q.; Dong, F. L.; Luo, F.; Li, C. Degradation of sulfonamides and formation of trihalomethanes by chlorination after pre-oxidation with Fe(VI). *J. Environ. Sci.* **2018**, *73*, 89−95.

(11) Sharma, V. K.; Ma, J.; He, C.; Kim, H.; Zboril, R. Ferrate(VI): A Green Molecule in Odorous Gas Treatment.. In *Green Catalysts for Energy Transformation and Emission Control*; American Chemical Society, 2014; Vol. *1184*, pp 193−207.

(12) Jiang, J. Q.; Wang, S.; Panagoulopoulos, A. The role of potassium ferrate(VI) in the inactivation of *Escherichia coli* and in the reduction of COD for water remediation. *Desalination* **2007**, *210*, 266−273.

(13) Liu, Y.; Wang, L.; Ma, J.; Zhao, X.; Huang, Z.; Mahadevan, G. D.; Qi, J. Improvement of settleability and dewaterability of sludge by newly prepared alkaline ferrate solution. *Chem. Eng. J.* **2016**, *287*, 11−18.

(14) Huang, H.; Sommerfeld, D.; Dunn, B.; Lloyd, C.; Eyring, E. Ferrate(VI) oxidation of aniline. *J. Chem. Soc., Dalton Trans.* **2001**, *8*, 1301−1305.

(15) Sun, S.; Liu, Y.; Ma, J.; Pang, S.; Huang, Z.; Gu, J.; Gao, Y.; Xue, M.; Yuan, Y.; Jiang, J. Transformation of substituted anilines by ferrate(VI): Kinetics, pathways, and effect of dissolved organic matter. *Chem. Eng. J.* **2018**, *332*, 245−252.

(16) Deng, S.; Bao, Y.; Cagnetta, G.; Huang, J.; Yu, G. Mechanochemical degradation of perfluorohexane sulfonate: Synergistic effect of ferrate(VI) and zero-valent iron. *Environ. Pollut.* **2020**, *264*, No. 114789.

(17) Xie, J. H.; Lo, P. K.; Lam, C. S.; Lau, K. C.; Lau, T. C. A hydrogen-atom transfer mechanism in the oxidation of alcohols by FeO4 (2-) in aqueous solution. *Dalton Trans.* **2018**, *47*, 240−245.

(18) Yu, H.; Chen, J.; Xie, H.; Ge, P.; Kong, Q.; Luo, Y. Ferrate(vi) initiated oxidative degradation mechanisms clarified by DFT calculations: a case for sulfamethoxazole. *Environ. Sci.: Processes Impacts.* **2017**, *19*, 370−378.

(19) Johnson, M. D.; Hornstein, B. J. The Kinetics and Mechanism of the Ferrate(VI) Oxidation of Hydroxylamines. *Inorg. Chem.* **2003**, *42*, 6923−6928.

(20) Kamachi, T.; Tomohisa, K.; Kazunari, Y. Participation of multioxidants in the pH dependence of the reactivity of ferrate(VI). *J. Org. Chem.* **2005**, *70*, 4380−4388.

(21) Yang, B.; Kookana, R. S.; Williams, M.; Ying, G.-G.; Du, J.; Doan, H.; Kumar, A. Oxidation of ciprofloxacin and enrofloxacin by ferrate(VI): Products identification, and toxicity evaluation. *J. Hazard. Mater.* **2016**, *320*, 296−303.

(22) Vagánek, A.; Rimarčík, J.; Ilčin, M.; Škorňa, P.; Lukeš, V.; Klein, E. Homolytic N−H bond cleavage in anilines: Energetics and substituent effect. *Comput. Theor. Chem.* **2013**, *1014*, 60−67.

(23) Yin, R.; Guo, W.; Ren, N.; Zeng, L.; Zhu, M. New insight into the substituents affecting the peroxydisulfate nonradical oxidation of sulfonamides in water. *Water Res.* **2020**, *171*, No. 115374.

(24) Bi, W.; Wang, F.; Han, J.; Liu, B.; Shen, J.; Zhang, L.; Okamoto, Y. Influence of the substituents on phenyl groups on enantioseparation property of amylose phenylcarbamates. *Carbohydr. Polym.* **2020**, *241*, No. 116372.

(25) Dar, A. A.; Chen, J.; Shad, A.; Pan, X.; Yao, J.; Bin-Jumah, M.; Allam, A. A.; Huo, Z.; Zhu, F.; Wang, Z. A combined experimental and computational study on the oxidative degradation of bromophenols by Fe(VI) and the formation of self-coupling products. *Environ. Pollut.* **2020**, *258*, No. 113678.

(26) Shehab, O. R.; Mansour, A. M. Exploring electronic structure, and substituent effect of some biologically active benzimidazole derivatives: Experimental insights and DFT calculations. *J. Mol. Struct.* **2021**, *1223*, No. 128996.

(27) Dostanić, J.; Huš, M.; Lončarević, D. Effect of substituents in hydroxyl radical-mediated degradation of azo pyridone dyes: Theoretical approaches on the reaction mechanism. *J. Environ. Sci.* **2020**, *98*, 14−21.

(28) Adamczyk-Woźniak, A.; Sporzyński, A. The influence of ortho-substituents on the properties of phenylboronic acids. *J. Organomet. Chem.* **2020**, *913*, No. 121202.

(29) Kamachi, T.; Miyanishi, M.; Yoshizawa, K. DFT Study on the pH Dependence of the Reactivity of Ferrate(VI). In *Ferrites and Ferrates: Chemistry and Applications in Sustainable Energy and Environmental Remediation*; American Chemical Society, 2016; Vol. *1238*, pp 473−487.

https://doi.org/10.1021/acsomega.1c01134
ACS Omega 2021, 6, 14317−14326

(30) Zhang, Y.; Moores, A.; Liu, J.; Ghoshal, S. New Insights into the Degradation Mechanism of Perfluorooctanoic Acid by Persulfate from Density Functional Theory and Experimental Data. *Environ. Sci. Technol.* **2019**, *53*, 8672−8681.
(31) Zhang, C.; Sun, T.; Sun, X. Mechanism for OH-Initiated Degradation of 2,3,7,8-Tetrachlorinated Dibenzo-p-Dioxins in the Presence of O2 and NO/H2O. *Environ. Sci. Technol.* **2011**, *45*, 4756−4762.
(32) Li, H.; Miao, X.; Zhang, J.; Du, J.; Xu, S.; Tang, J.; Zhang, Y. DFT studies on the reaction mechanism and kinetics of dibutyl phthalate initiated by hydroxyl and sulfate radicals: Prediction of the most reactive sites. *Chem. Eng. J.* **2020**, *381*, No. 122680.
(33) von Sonntag, C.; von Gunten, U. *Chemistry of Ozone in Water and Wastewater Treatment: From Basic Principles to Applications*; IWA Publishing: 2012; pp 132−142.
(34) O'Neill, F. J.; Bromley-Challenor, K. C. A.; Greenwood, R. J.; Knapp, J. S. Bacterial growth on aniline: implications for the biotreatment of industrial wastewater. *Water Res.* **2000**, *34*, 4397−4409.
(35) Sharma, V. K.; Liu, F.; Tolan, S.; Sohn, M.; Kim, H.; Oturan, M. A. Oxidation of β-lactam antibiotics by ferrate(VI). *Chem. Eng. J.* **2013**, *221*, 446−451.
(36) Norcross, B. E.; Lewis, W. C.; Gai, H.; Noureldin, N. A.; Lee, D. G. The oxidation of secondary alcohols by potassium tetraoxoferrate(VI). *Can. J. Chem.* **1997**, *75*, 129−139.
(37) Frisch, M. J.; Trucks, G. W.; Schlegel, H. B.; Scuseria, G. E.; Robb, M. A.; Cheeseman, J. R.; Scalmani, G.; Barone, V.; Petersson, G. A.; Nakatsuji, H.; Li, X.; Caricato, M.; Marenich, A. V.; Bloino, J.; Janesko, B. G.; Gomperts, R.; Mennucci, B.; Hratchian, H. P.; Ortiz, J. V.; Izmaylov, A. F.; Sonnenberg, J. L.; Williams; Ding, F.; Lipparini, F.; Egidi, F.; Goings, J.; Peng, B.; Petrone, A.; Henderson, T.; Ranasinghe, D.; Zakrzewski, V. G.; Gao, J.; Rega, N.; Zheng, G.; Liang, W.; Hada, M.; Ehara, M.; Toyota, K.; Fukuda, R.; Hasegawa, J.; Ishida, M.; Nakajima, T.; Honda, Y.; Kitao, O.; Nakai, H.; Vreven, T.; Throssell, K.; Montgomery, J. A., Jr.; Peralta, J. E.; Ogliaro, F.; Bearpark, M. J.; Heyd, J. J.; Brothers, E. N.; Kudin, K. N.; Staroverov, V. N.; Keith, T. A.; Kobayashi, R.; Normand, J.; Raghavachari, K.; Rendell, A. P.; Burant, J. C.; Iyengar, S. S.; Tomasi, J.; Cossi, M.; Millam, J. M.; Klene, M.; Adamo, C.; Cammi, R.; Ochterski, J. W.; Martin, R. L.; Morokuma, K.; Farkas, O.; Foresman, J. B.; Fox, D. J. *Gaussian 16* rev. C.01; Wallingford, CT, 2016.
(38) Sun, Y.; Tang, H.; Chen, K.; Hu, L.; Yao, J.; Shaik, S.; Chen, H. Two-State Reactivity in Low-Valent Iron-Mediated C−H Activation and the Implications for Other First-Row Transition Metals. *J. Am. Chem. Soc.* **2016**, *138*, 3715−3730.
(39) Wang, X.; Wang, Y.; Chen, J.; Ma, Y.; Zhou, J.; Fu, Z. Computational Toxicological Investigation on the Mechanism and Pathways of Xenobiotics Metabolized by Cytochrome P450: A Case of BDE-47. *Environ. Sci. Technol.* **2012**, *46*, 5126−5133.
(40) Ji, Y.; Lu, J.; Wang, L.; Jiang, M.; Yang, Y.; Yang, P.; Zhou, L.; Ferronato, C.; Chovelon, J.-M. Non-activated peroxymonosulfate oxidation of sulfonamide antibiotics in water: Kinetics, mechanisms, and implications for water treatment. *Water Res.* **2018**, *147*, 82−90.
(41) Fukuyo, M.; Hirotsu, K.; Higuchi, T. The Structure of Aniline at 252-k. *Acta Crystallogr., Sect. B: Struct. Crystallogr. Cryst. Chem.* **1982**, *38*, 640−643.
(42) Ouellette, R. J.; Rawn, J. D. 25 - Aryl Halides, Phenols, and Anilines. In *Organic Chemistry*; 2nd ed.; Ouellette, R. J.; Rawn, J. D., Eds.; Academic Press, 2018; pp 801−828.
(43) Marcus, R. A. Electron Transfer Reactions in Chemistry: Theory and Experiment (Nobel Lecture). *Angew. Chem., Int. Ed. Engl.* **1993**, *32*, 1111−1121.
(44) Feng, M.; Baum, J. C.; Nesnas, N.; Lee, Y.; Huang, C. H.; Sharma, V. K. Oxidation of Sulfonamide Antibiotics of Six-Membered Heterocyclic Moiety by Ferrate(VI): Kinetics and Mechanistic Insight into SO2 Extrusion. *Environ. Sci. Technol.* **2019**, *53*, 2695−2704.
(45) Zhao, L.; Kaiser, R. I.; Lu, W.; Xu, B.; Ahmed, M.; Morozov, A. N.; Mebel, A. M.; Howlader, A. H.; Wnuk, S. F. Molecular mass growth through ring expansion in polycyclic aromatic hydrocarbons via radical−radical reactions. *Nat. Commun.* **2019**, *10*, No. 3689.
(46) Krasnoukhov, V. S.; Zagidullin, M. V.; Zavershinskiy, I. P.; Mebel, A. M. Formation of Phenanthrene via Recombination of Indenyl and Cyclopentadienyl Radicals: A Theoretical Study. *J. Phys. Chem. A* **2020**, *124*, 9933−9941.
(47) Luo, C.; Feng, M.; Sharma, V. K.; Huang, C.-H. Revelation of ferrate(VI) unimolecular decay under alkaline conditions: Investigation of involvement of Fe(IV) and Fe(V) species. *Chem. Eng. J.* **2020**, *388*, No. 124134.
(48) Chen, W.-S.; Shih, Y.-C. Mineralization of aniline in aqueous solution by sono-activated peroxydisulfate enhanced with PbO semiconductor. *Chemosphere* **2020**, *239*, No. 124686.
(49) Pang, S.-Y.; Duan, J.-B.; Zhou, Y.; Gao, Y.; Jiang, J. Oxidation kinetics of anilines by aqueous permanganate and effects of manganese products: Comparison to phenols. *Chemosphere* **2019**, *235*, 104−112.
(50) Sang, W.; Cui, J.; Feng, Y.; Mei, L.; Zhang, Q.; Li, D.; Zhang, W. Degradation of aniline in aqueous solution by dielectric barrier discharge plasma: Mechanism and degradation pathways. *Chemosphere* **2019**, *223*, 416−424.
(51) Chen, G.; Lam, W. W. Y.; Lo, P. K.; Man, W. L.; Chen, L. J.; Lau, K. C.; Lau, T. C. Mechanism of Water Oxidation by Ferrate(VI) at pH 7-9. *Chem. - Eur. J.* **2018**, *24*, 18735−18742.
(52) Terryn, R. J.; Huerta-Aguilar, C. A.; Baum, J. C.; Sharma, V. K. FeVI, FeV, and FeIV oxidation of cyanide: Elucidating the mechanism using density functional theory calculations. *Chem. Eng. J.* **2017**, *330*, 1272−1278.
(53) Sharma, V. K.; Yngard, R. A.; Cabelli, D. E.; Clayton Baum, J. Ferrate(VI) and ferrate(V) oxidation of cyanide, thiocyanate, and copper(I) cyanide. *Radiat. Phys. Chem.* **2008**, *77*, 761−767.
(54) Sharma, V. K. Oxidation of inorganic contaminants by ferrates (VI, V, and IV)−kinetics and mechanisms: A review. *J. Environ. Manage.* **2011**, *92*, 1051−1073.
(55) Sarma, R.; Angeles-Boza, A. M.; Brinkley, D. W.; Roth, J. P. Studies of the Di-iron(VI) Intermediate in Ferrate-Dependent Oxygen Evolution from Water. *J. Am. Chem. Soc.* **2012**, *134*, 15371−15386.
(56) Chen, G.; Lam, W. W. Y.; Lo, P.-K.; Man, W.-L.; Chen, L.; Lau, K.-C.; Lau, T.-C. Mechanism of Water Oxidation by Ferrate(VI) at pH7−9. *Chem. - Eur. J.* **2018**, *24*, 18735−18742.
(57) Yu, H.; Ge, P.; Chen, J.; Xie, H.; Luo, Y. The degradation mechanism of sulfamethoxazole under ozonation: a DFT study. *Environ. Sci.: Processes Impacts.* **2017**, *19*, 379−387.
(58) Kang, X.; Song, Y.; Luo, Y.; Li, G.; Hou, Z.; Qu, J. Computational Studies on Isospecific Polymerization of 1-Hexene Catalyzed by Cationic Rare Earth Metal Alkyl Complex Bearing a C3iPr-trisox Ligand. *Macromolecules* **2012**, *45*, 640−651.
(59) Kang, X.; Luo, Y.; Zhou, G.; Wang, X.; Yu, X.; Hou, Z.; Qu, J. Theoretical Mechanistic Studies on the trans-1,4-Specific Polymerization of Isoprene Catalyzed by a Cationic La−Al Binuclear Complex. *Macromolecules* **2014**, *47*, 4596−4606.
(60) Koizumi, K.; Yamaguchi, K.; Nakamura, H.; Takano, Y. Hybrid-DFT Study on Electronic Structures of the Active Site of Sweet Potato Purple Acid Phosphatase: The Origin of Stronger Antiferromagnetic Couplings than Other Purple Acid Phosphatases. *J. Phys. Chem. A* **2009**, *113*, 5099−5104.
(61) Sebetci, A.; Richter, M. Gd@C82: Origin of the Antiferromagnetic Coupling between Endohedral Gd and the Free Spin on the Carbon Cage. *J. Phys. Chem. C* **2010**, *114*, 15−19.
(62) Abdel-Rahman, M. A.; Shibl, M. F.; El-Demerdash, S. H.; El-Nahas, A. M. Simulated kinetics of the atmospheric removal of aniline during daytime. *Chemosphere* **2020**, *255*, No. 127031.
(63) Jaeger, M.; Aspers, R. L. E. G. Chapter Three - Steroids and NMR. In *Annual Reports on NMR Spectroscopy*; Webb, G. A., Ed.; Academic Press, 2012; Vol. *77*, pp 115−258.

https://doi.org/10.1021/acsomega.1c01134
ACS Omega 2021, 6, 14317−14326